Supporting Information

A fluorescence "turn-on" chemosensor for Hg^{2+} and Ag^{+} based on NBD (7-nitrobenzo-2-oxa-1,3-diazolyl)

Seong Youl Lee, Kwon Hee Bok, Cheal Kim*

Department of Fine Chemistry and Department of Interdisciplinary Bio IT Materials, Seoul National University of Science and Technology, Seoul 139-743, Korea. Fax: +82-2-973-9149; Tel: +82-2-970-6693; E-mail: chealkim@seoultech.ac.kr

Table S1. Examples of chemosensors for simultaneous detection of Hg^{2+} and Ag^{+}.

Sensor	Detection limit (Hg^{2+}/Ag^{+}, μM)	Binding constant (Hg^{2+}/Ag^{+}, M^{-1})	Percent of water in solution (%)	Method of detection (Hg^{2+}/Ag^{+})	Reference
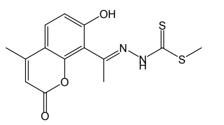	0.29 / 0.4	2.3×10^{4} / 5.1×10^{4}	50	Fluorescence	1
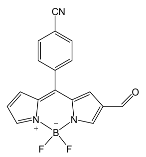	140 / 650	No data	15	Fluorescence, Colorimetric	2
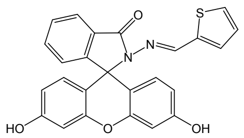	0.21 / 0.009	2.2×10^{4} / No data	40	Fluorescence	3
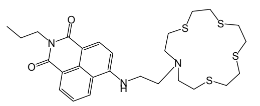	0.25 / No data	7.4×10^{8} / No data	80	Fluorescence	4
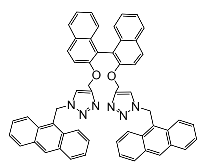	No data	1.0×10^{9} / 4.1×10^{4}	0.5	Fluorescence	5
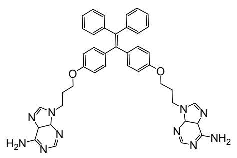	0.37 / 0.34	2.6×10^{5} / No data	67	Fluorescence	6
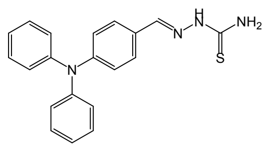	0.19 / 0.59	1.0×10^{5} / 9.4×10^{4}	10	Fluorescence	7
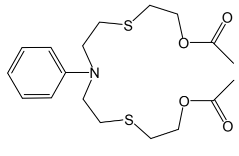	0.13 / No data	3.1×10^{3} / 1.2×10^{8}	50	Fluorescence, Colorimetric	8
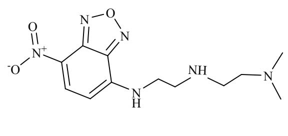	0.05 / 0.12	5.0×10^{4} / 3.5×10^{4}	70	Fluorescence	This work

References

1 H. El-Shekheby, A. H. Mangood, S. M. Hamza, A. S. Al-Kady and E.-Z. M. Ebeid, *Luminescence*, 2014, **29**, 158-167.

2 X. Zhang, Y. Xu, P. Guo and X. Qian, *New J. Chem.*, 2012, **36**, 1621-1625.

3 W. Shen, L. Wang, M. Wu and X. Bao, *Inorg. Chem. Commun.*, 2016, **70**, 107-110.

4 T. Chen, W. Zhu, Y. Xu, S. Zhang, X. Zhang and X. Qian, *Dalton Trans.*, 2010, **39**, 1316-1320.

5 X. Liu, X. Yang, H. Peng, C. Zhu and Y. Cheng, *Tetrahedron Lett.*, 2011, **52**, 2295-2298.

6 L. Liu, G. Zhang, J. Xiang, D. Zhang and D. Zhu, *Org. Lett.*, 2008, **10**, 4581-4584.

7 W. Shi, Y. Chen, X. Chen, Z. Xie and Y. Hui, *J. Lumin.*, 2016, **174**, 56-62.

8 J. Fan, C. Chen, Q. Lin and N. Fu, *Sens. Actuators B*, 2012, **173**, 874-881.

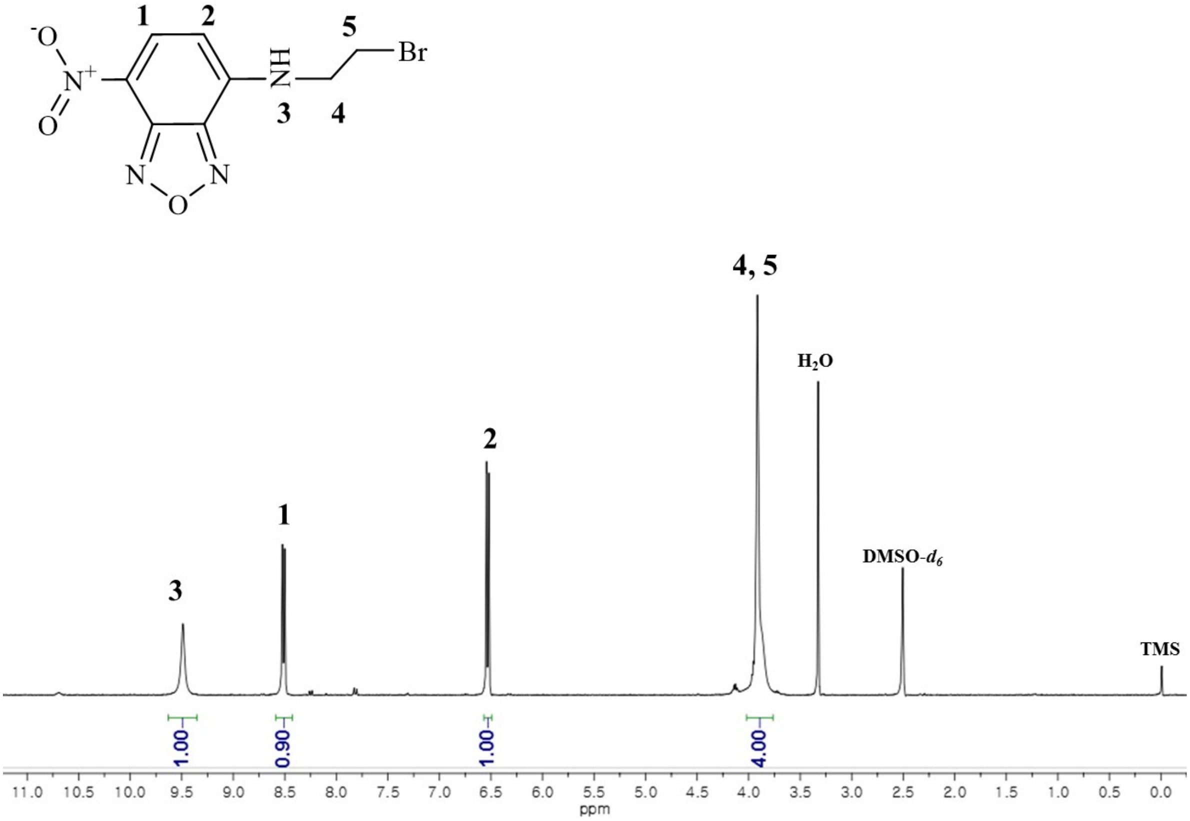

Fig. S1 ^{1}H NMR spectrum of **2**.

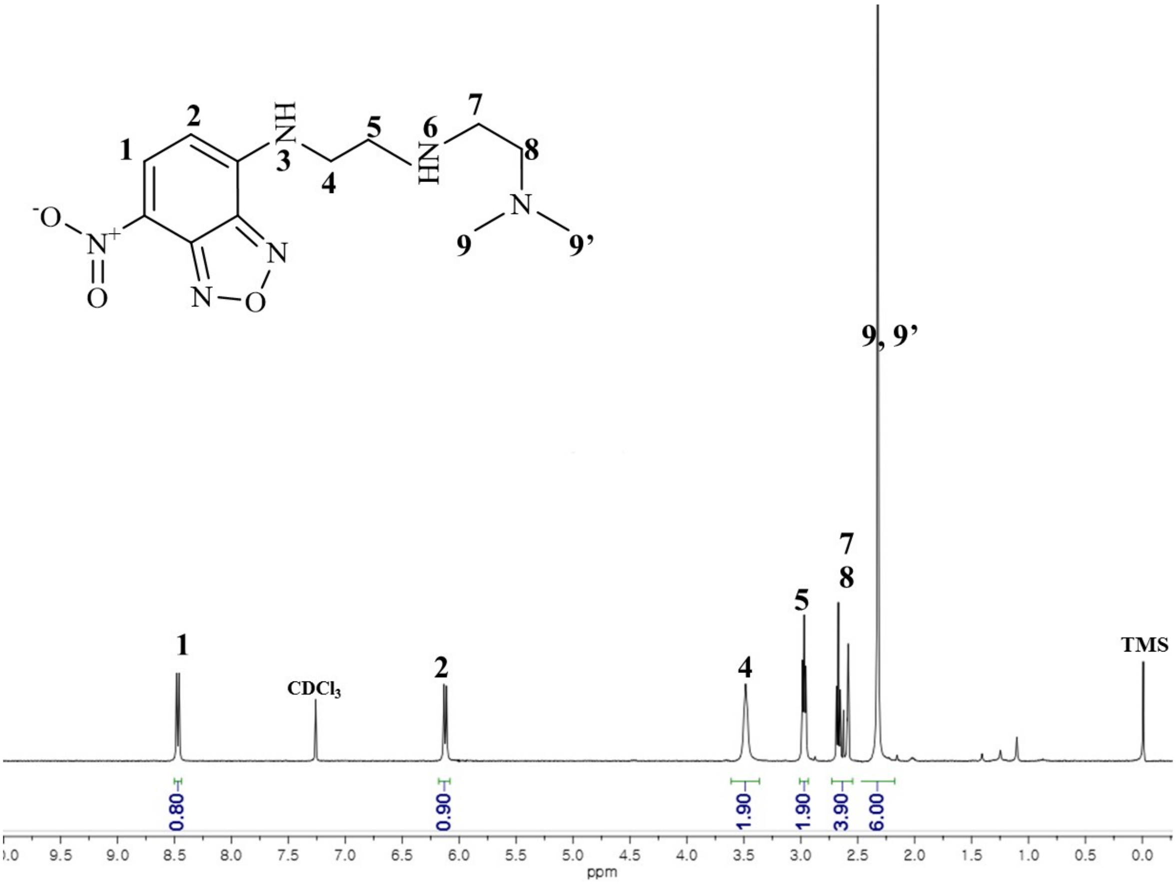

Fig. S2 ^{1}H NMR spectrum of **1**.

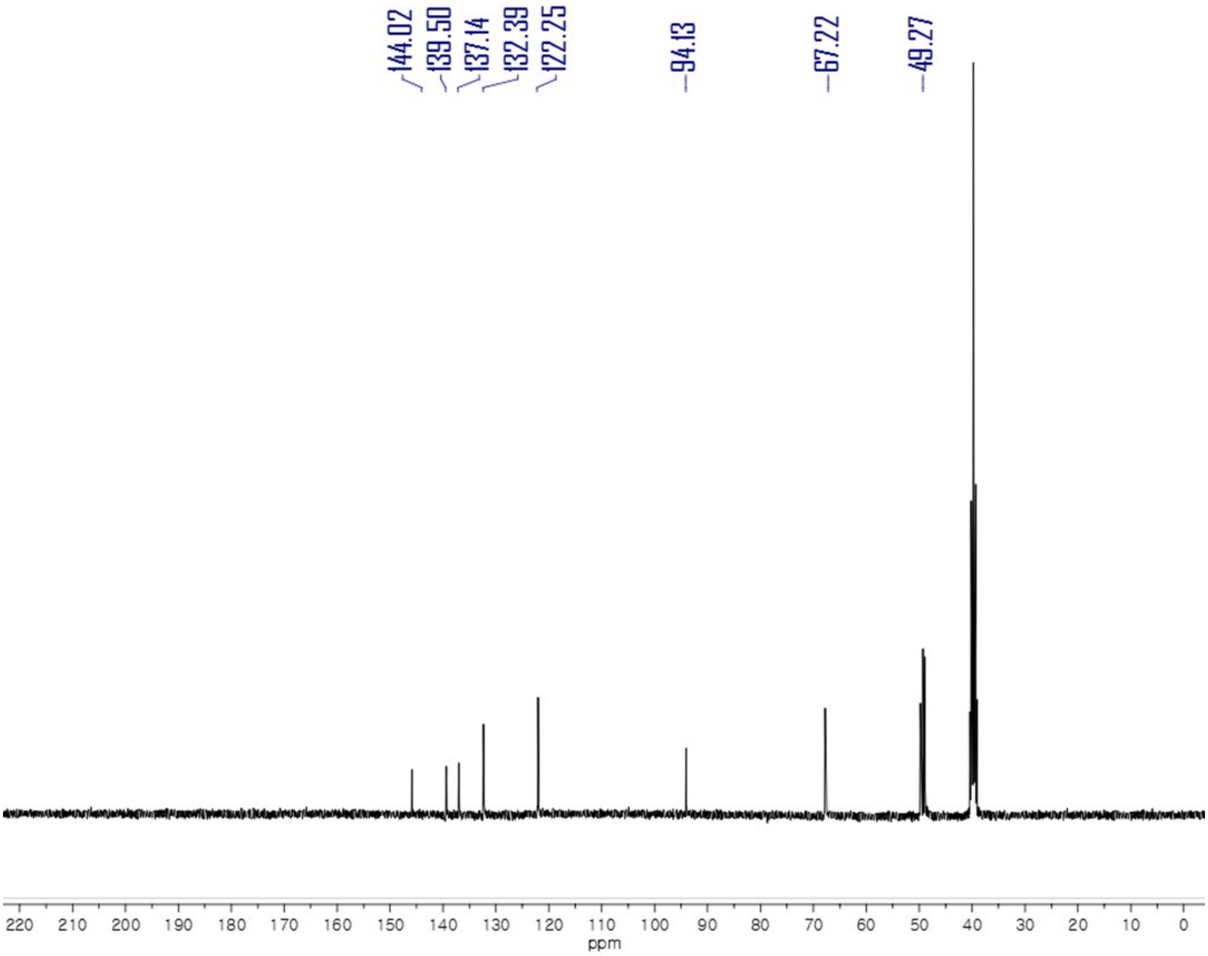

Fig. S3 ^{13}C NMR spectrum of **1**.

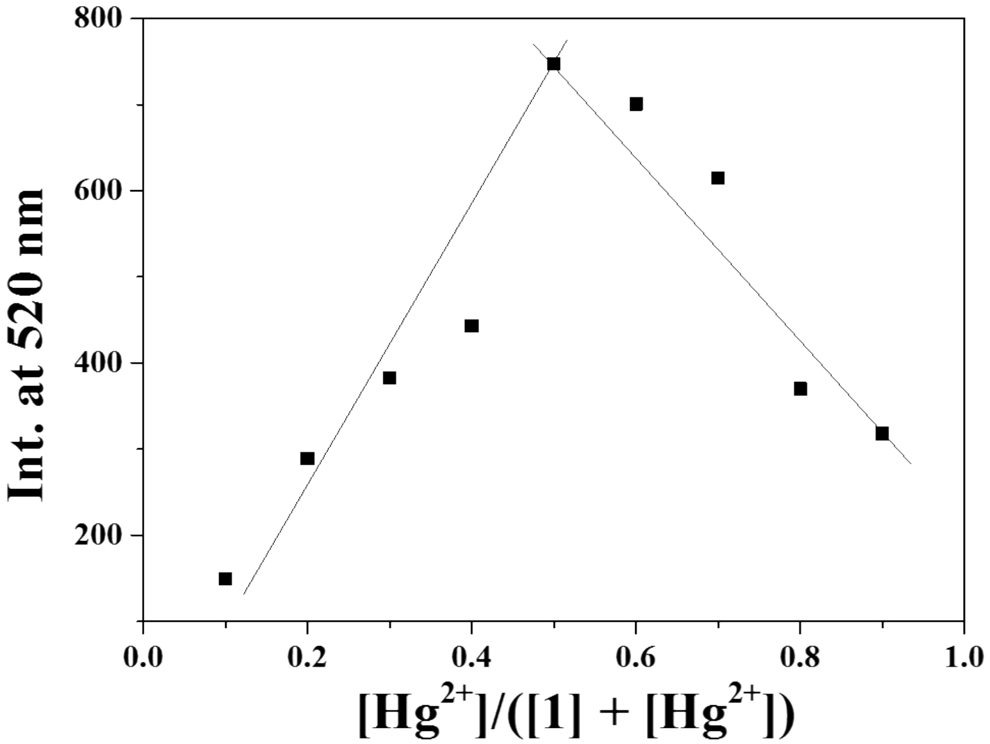

Fig. S4 Job plot of **1** and Hg^{2+}. The total concentrations of **1** and Hg^{2+} were 20 μM.

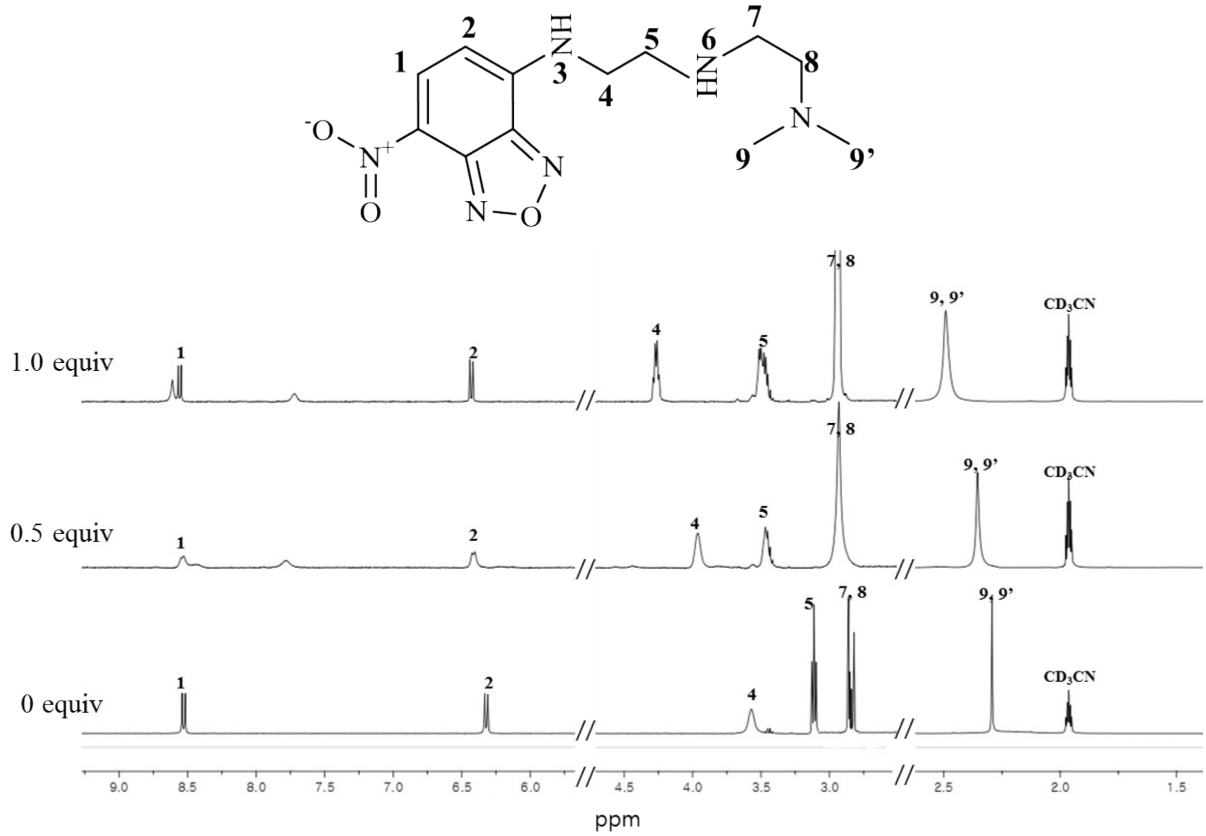

Fig. S5 ^{1}H NMR titration of **1** with Hg^{2+} ions.

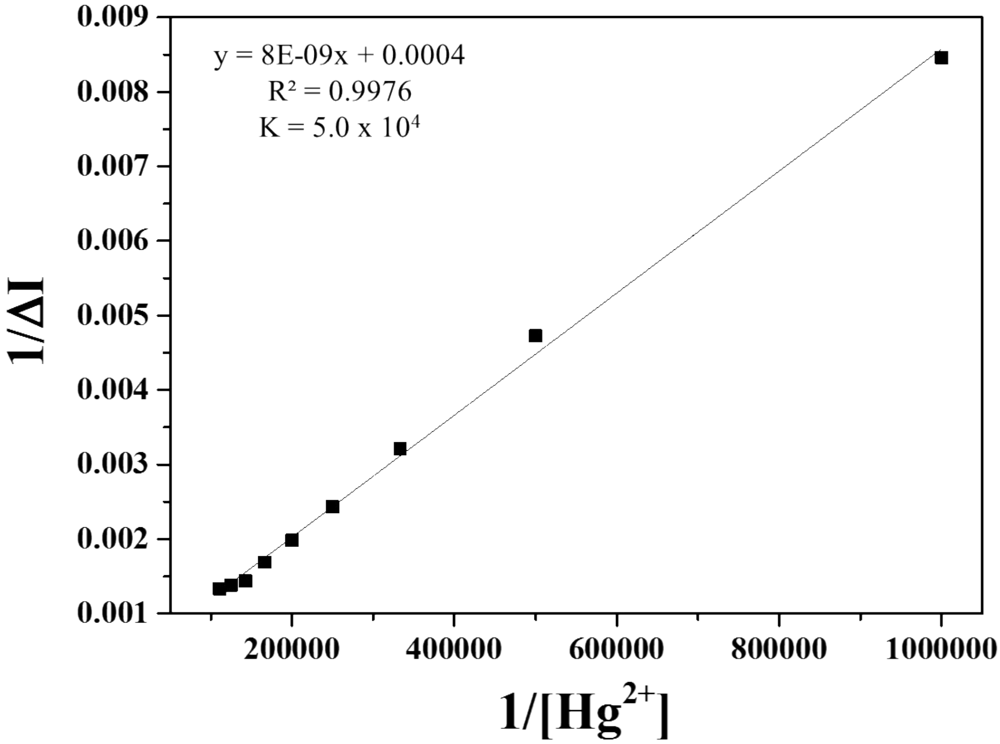

Fig. S6 Benesi-Hildebrand plot (at 520 nm) of **1** based on fluorescence titration, assuming 1:1 stoichiometry for association between **1** and Hg^{2+}.

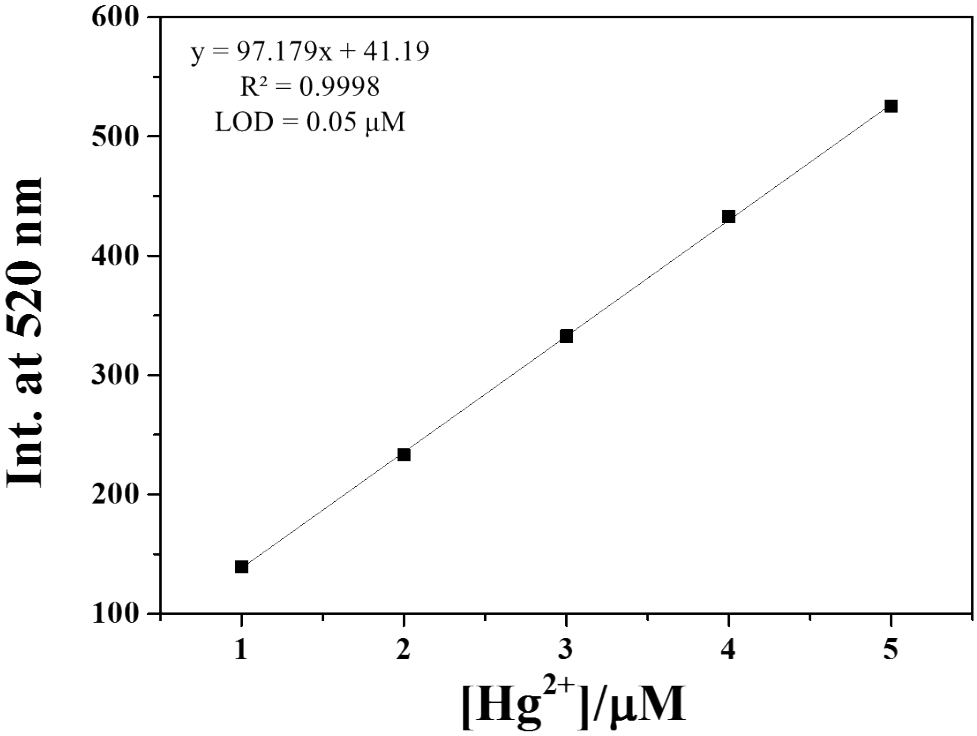

Fig. S7 Determination of the detection limit based on change in the ratio of **1** (5 μM) with Hg^{2+}.

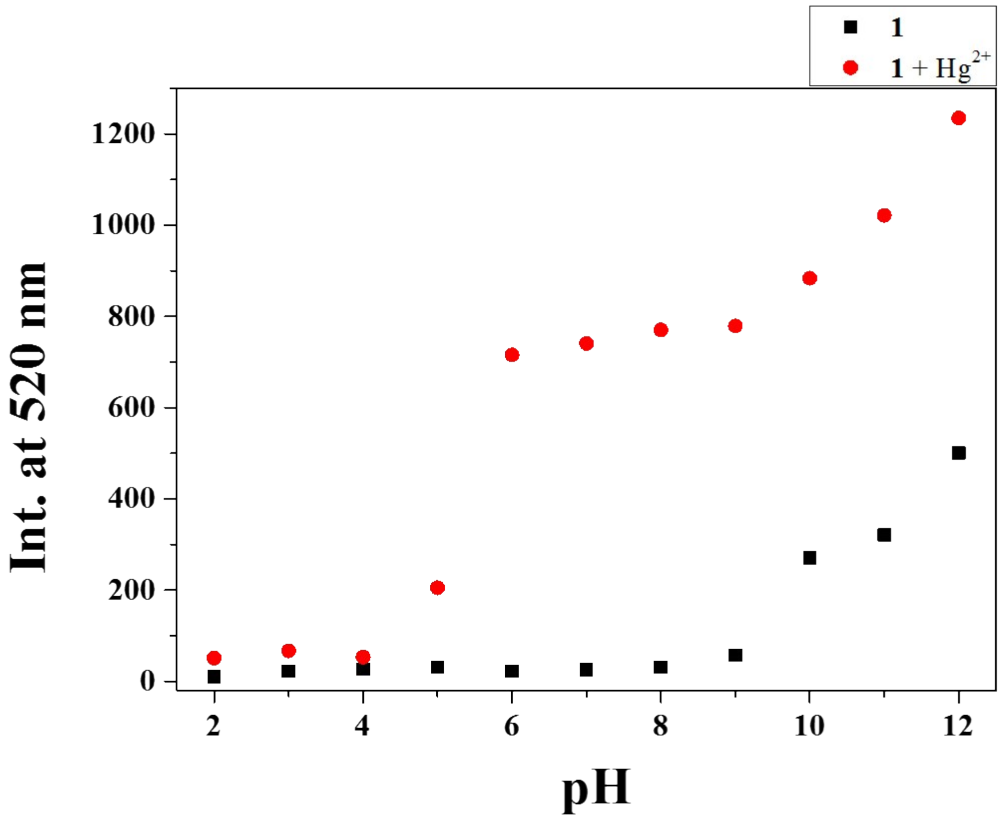

Fig. S8 Fluorescence intensities (520 nm) of **1** (5 μM) and **1**-Hg^{2+} complex, respectively, at pH 2-12 in a mixture of buffer-CH_3CN (7:3, v/v) at room temperature.

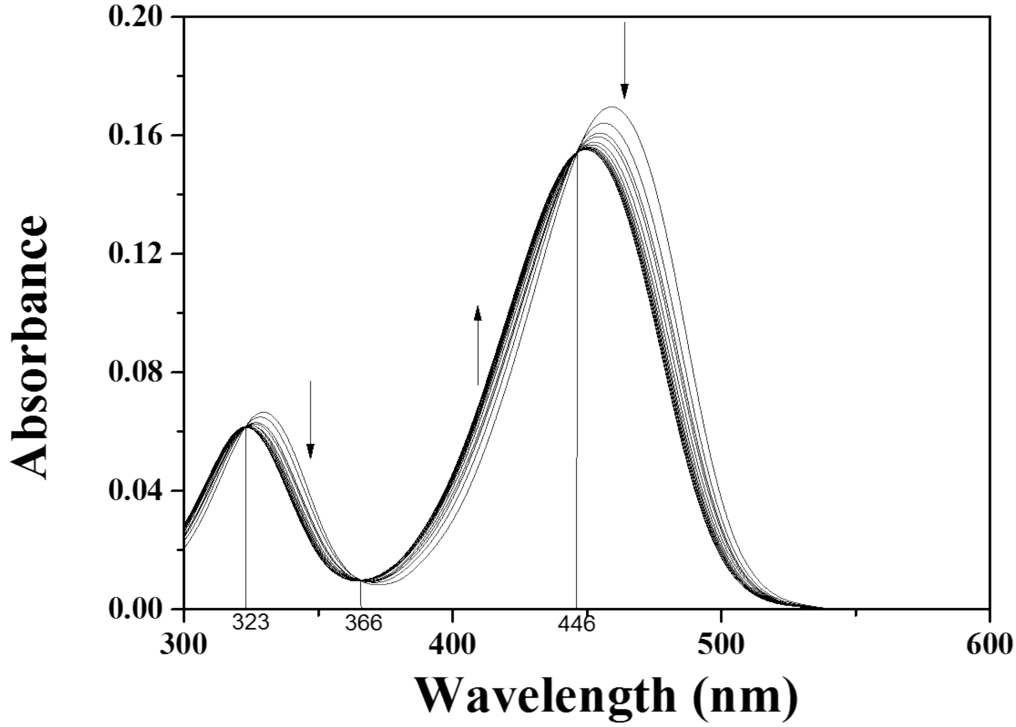

Fig. S9 Absorption spectral changes of **1** (5 μM) in the presence of different concentrations of Ag^{+} ions in a mixture of buffer-CH_3CN (7:3, v/v) at room temperature.

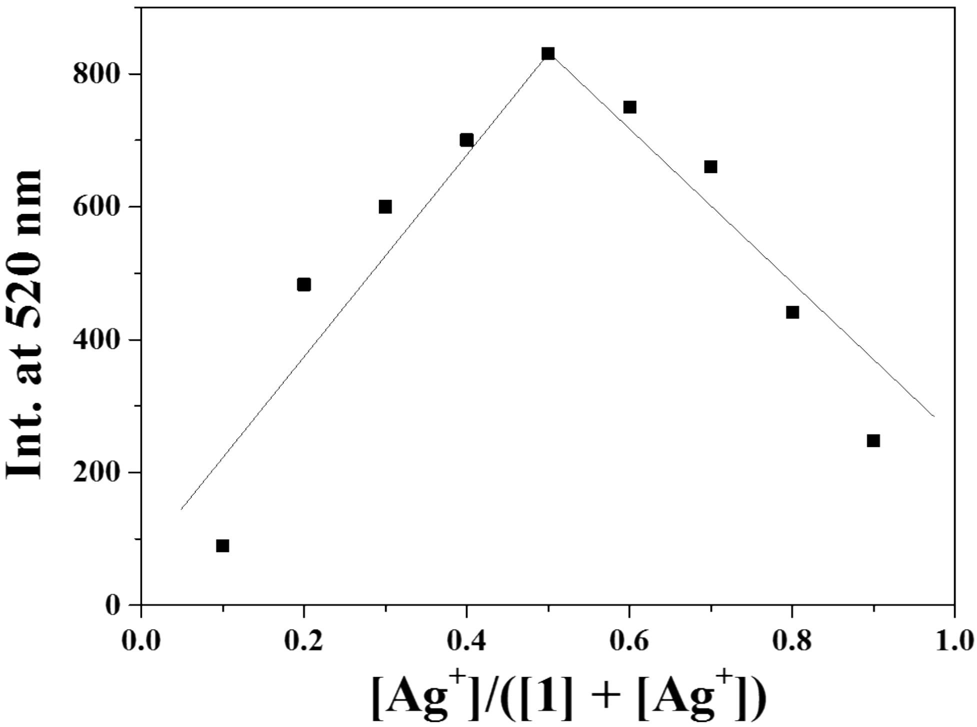

Fig. S10 Job plot of **1** and Ag^+. The total concentrations of **1** and Ag^+ were 20 μM.

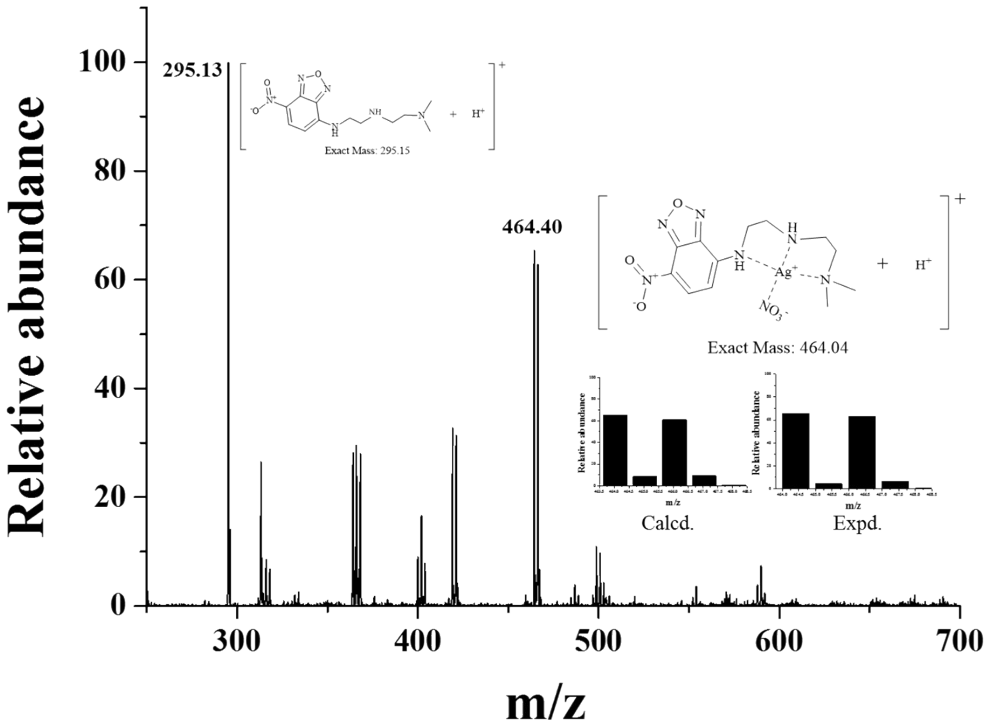

Fig. S11 Positive-ion electrospray ionization mass spectrum of **1** (10 μM) upon addition of $AgNO_3$ (1.0 equiv).

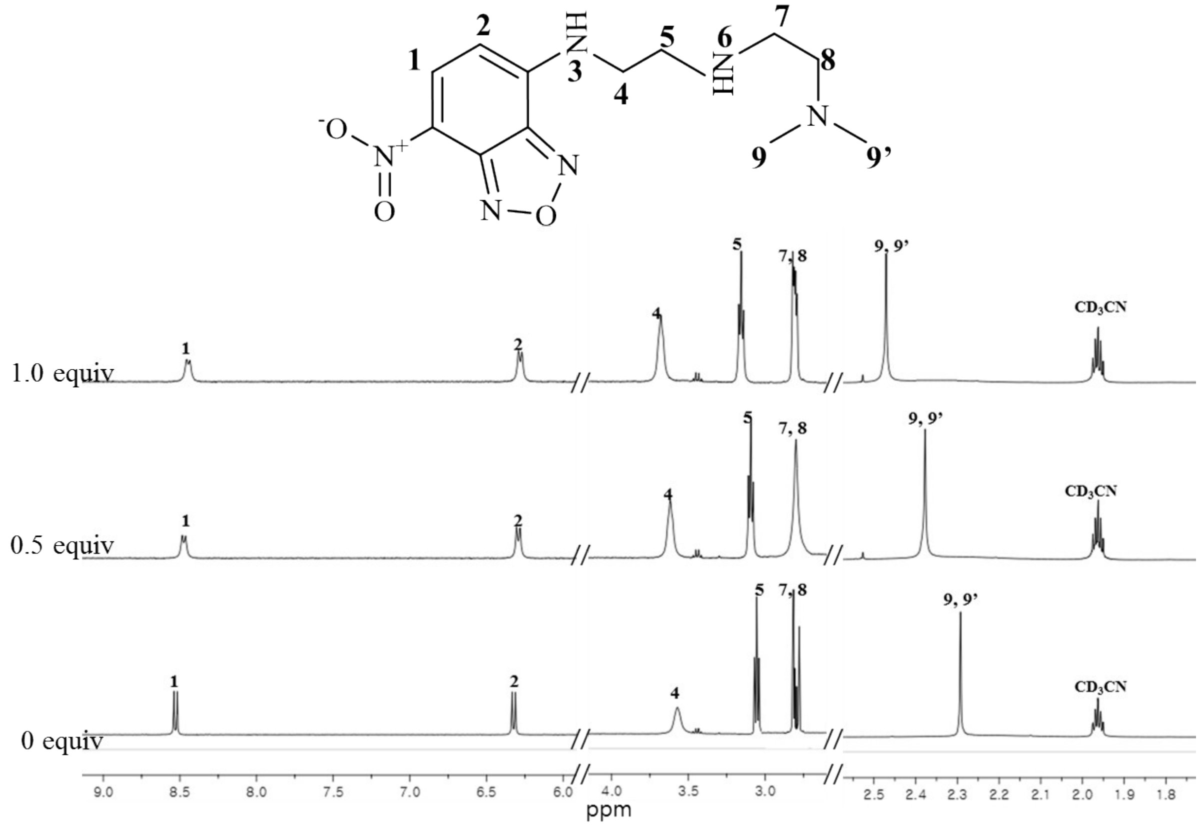

Fig. S12 ^{1}H NMR titration of **1** with Ag^+ ions.

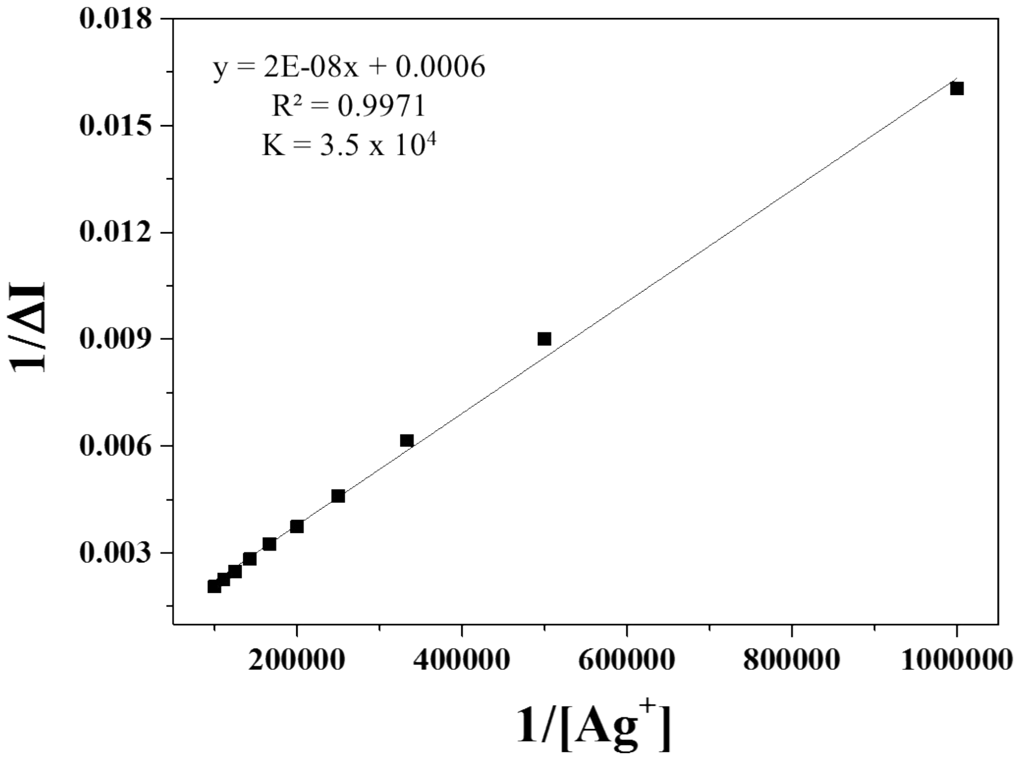

Fig. S13 Benesi-Hildebrand plot (at 520 nm) of **1** based on fluorescence titration, assuming 1:1 stoichiometry for association between **1** and Ag^+.

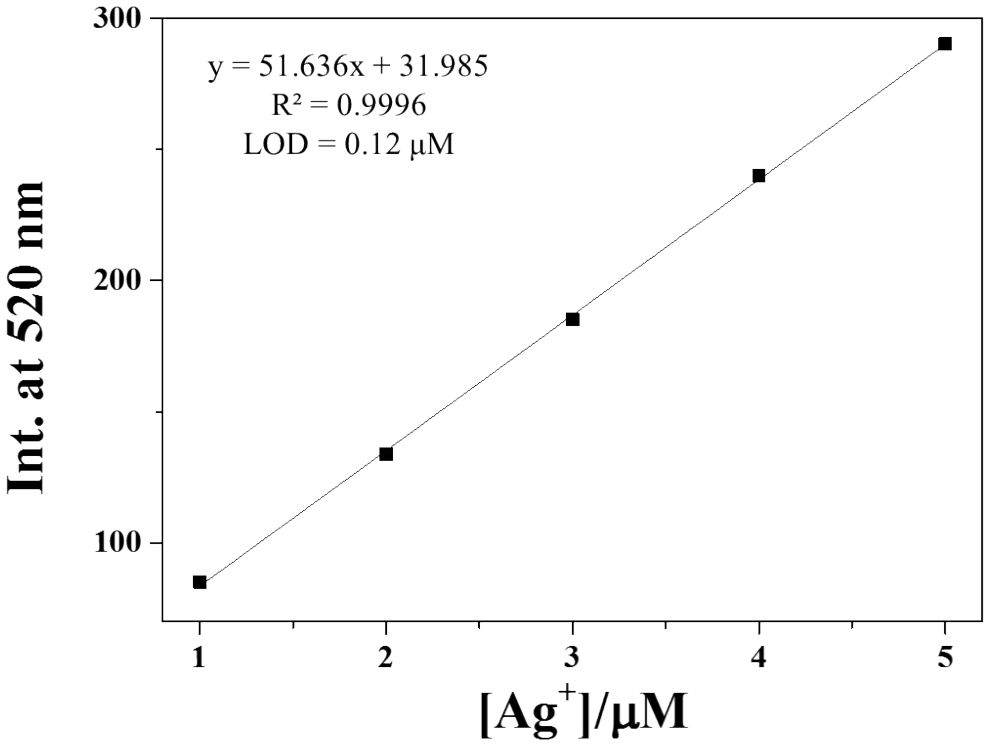

Fig. S14 Determination of the detection limit based on change in the ratio of **1** (5 μM) with Ag^{+}.

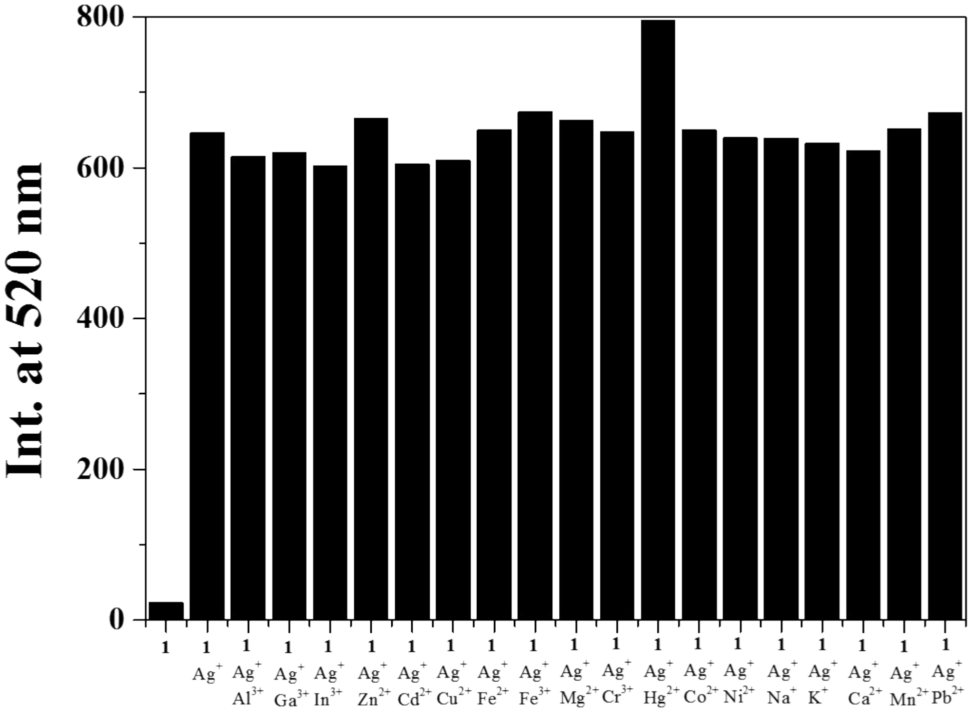

Fig. S15 Competitive selectivity of **1** (5 μM) toward Ag^+ (2.6 equiv) in the presence of other metal ions (2.6 equiv).

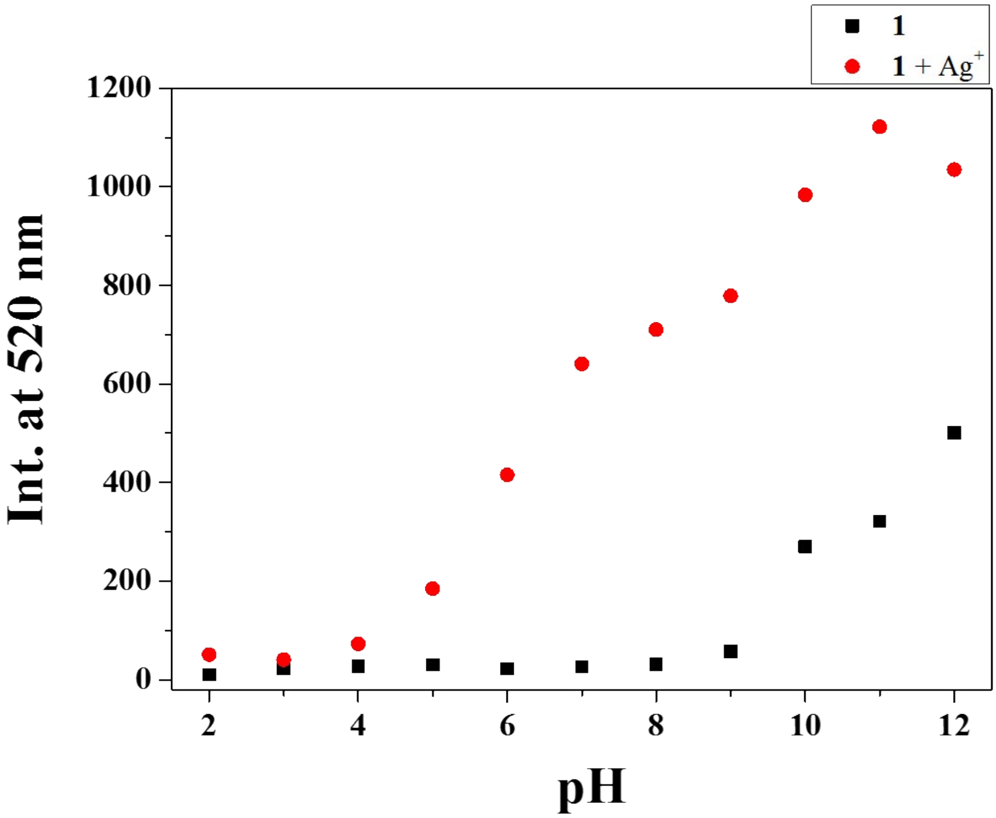

Fig. S16 Fluorescence intensities (520 nm) of **1** (5 μM) and **1**-Ag^{+} complex, respectively, at pH 2-12 in a mixture of buffer-CH_3CN (7:3, v/v) at room temperature.

(a)

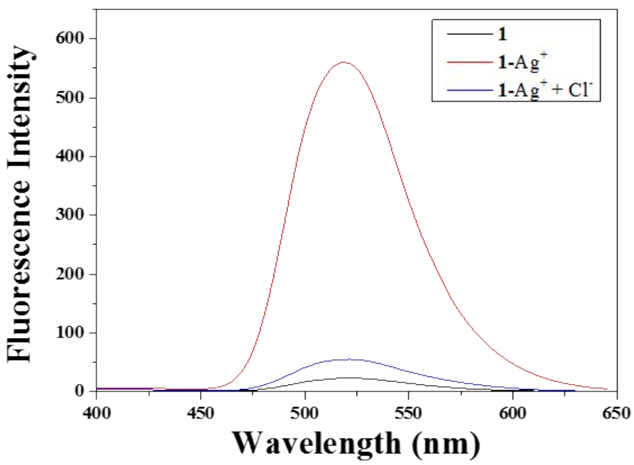

(b)

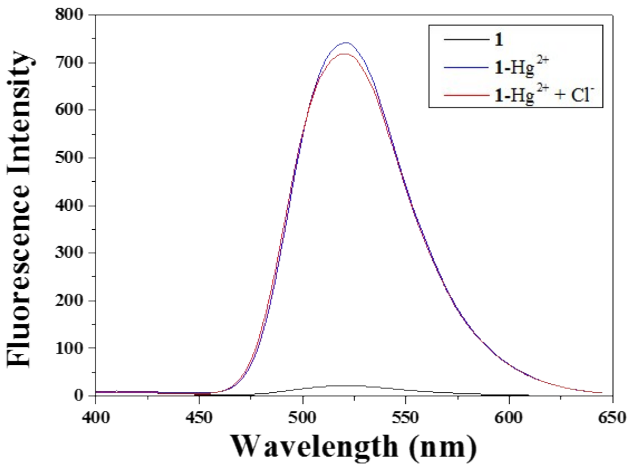

Fig. S17 Fluorescence spectral changes of **1** (5 μM) after the sequential addition of (a) Ag^{+} and Cl^{-}, and (b) Hg^{2+} and Cl^{-}.

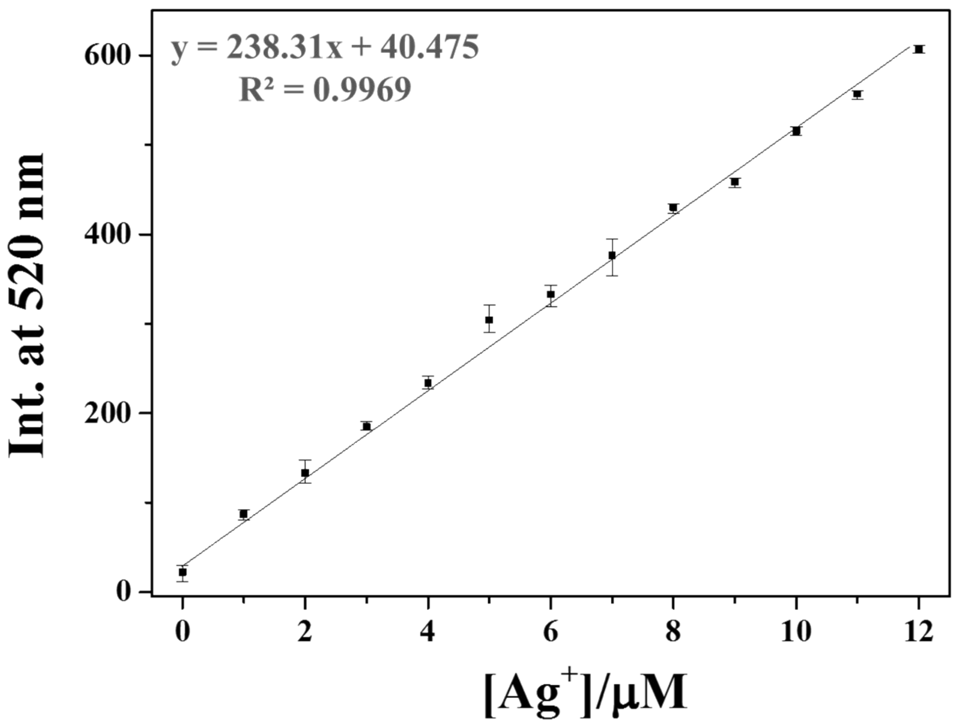

Fig. S18 Emission intensity (520 nm) of **1** as a function of Ag^+ concentration. [**1**] = 5 μmol/L and $[Ag^+]$ = 0.0-12.0 μmol/L in buffer-CH_3CN mixture (7:3, v/v).

(a)

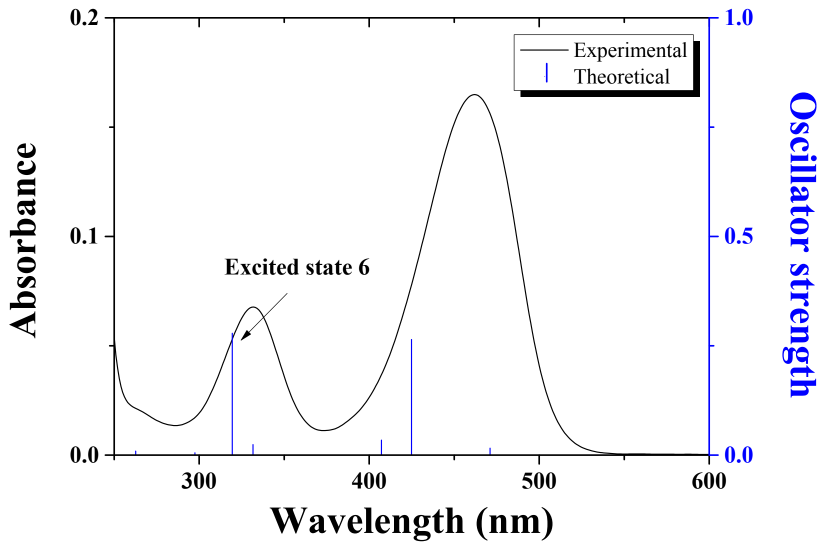

(b)

Excited state 6	Wavelength (nm)	Percent (%)	Main character	Oscillator strength
H - 1 → L + 1	319.45	93	PET	0.2788

Fig. S19 (a) The theoretical excitation energies and the experimental UV-vis spectrum of **1**. (b) The major electronic transition energies and molecular orbital contributions for **1** (H = HOMO and L = LUMO).

(a)

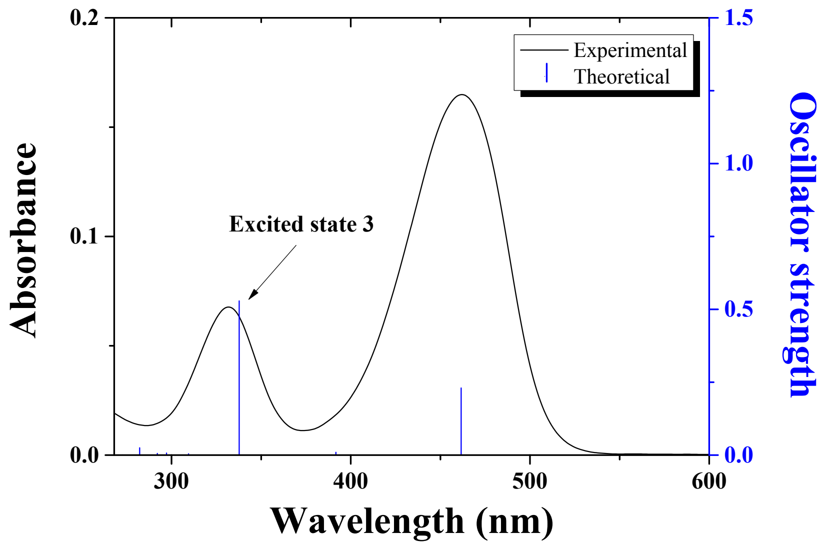

(b)

Excited state 3	Wavelength (nm)	Percent (%)	Main character	Oscillator strength
H → L + 2	337.73	83	Inhibited PET, π → π*	0.5289

Fig. S20 (a) The theoretical excitation energies and the experimental UV-vis spectrum of **1**-Hg^{2+}. (b) The major electronic transition energies and molecular orbital contributions for **1**-Hg^{2+} (H = HOMO and L = LUMO).

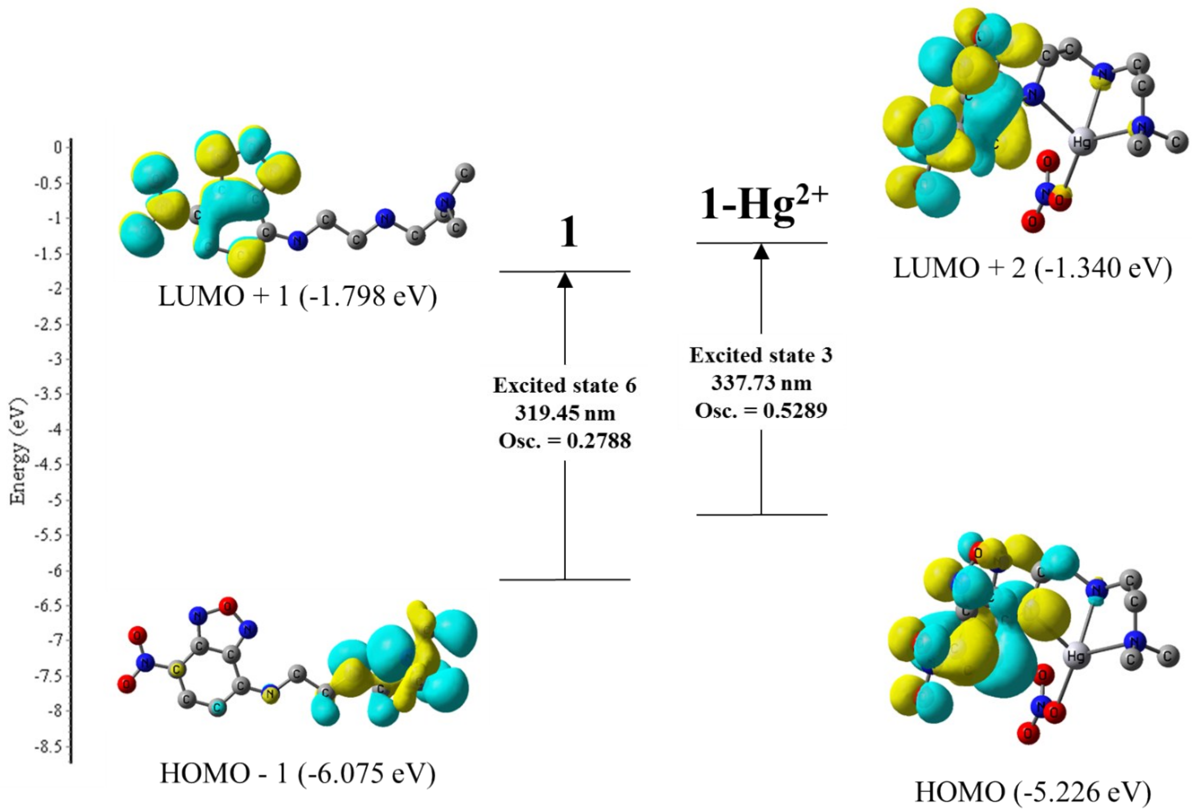

Fig. S21 Molecular orbital diagrams and excitation energies of **1** and **1**-Hg^{2+} complex.

(a)

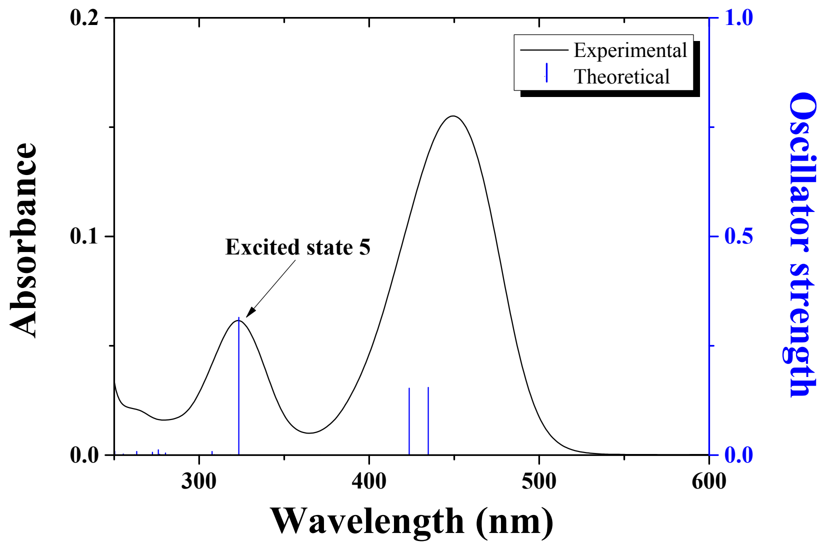

(b)

Excited state 5	Wavelength (nm)	Percent (%)	Main character	Oscillator strength
H → L + 1	323.28	94	Inhibited PET, π → π*	0.3149

Fig. S22 (a) The theoretical excitation energies and the experimental UV-vis spectrum of **1**-Ag^{+}. (b) The major electronic transition energies and molecular orbital contributions for **1**-Ag^{+} (H = HOMO and L = LUMO).

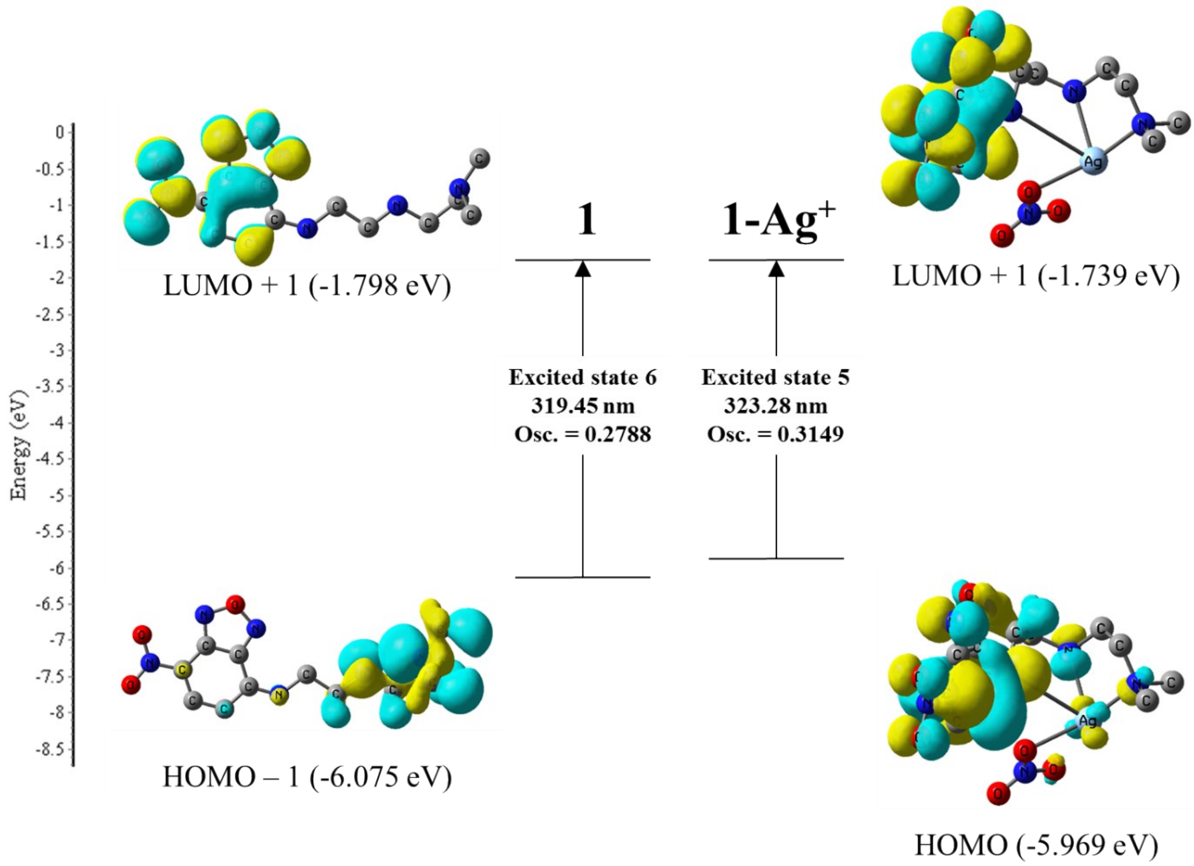

Fig. S23 Molecular orbital diagrams and excitation energies of **1** and **1**-Ag^+ complex.